Article:

Zhu, Y., Ekren, D., Cao, J. et al. (2024) Effect of graphene oxide and carbon black on the thermoelectric performance of niobium doped strontium titanate. Journal of Alloys and Compounds, 988. 174242. ISSN: 0925-8388

https://doi.org/10.1016/j.jallcom.2024.174242

Journal of Alloys and Compounds 988 (2024) 174242

Contents lists available at ScienceDirect

Journal of Alloys and Compounds

journal homepage: www.elsevier.com/locate/jalcom

Effect of graphene oxide and carbon black on the thermoelectric performance of niobium doped strontium titanate

Yibing Zhu [a], Dursun Ekren [a], Jianyun Cao [a], Xiaodong Liu [a], Stephanie R. Mudd [b], Rebecca Boston [b], Xiuqi Xia [a], Yi Li [a], Ian A. Kinloch [a,c], David J. Lewis [a,*], Robert Freer [a,*]

[a] *Department of Materials, The University of Manchester, Manchester M13 9PL, UK*
[b] *Department of Materials Science, The University of Sheffield, Sheffield S10 2TN, UK*
[c] *Henry Royce Institute and National Graphene Institute, University of Manchester, Manchester M13 9PL, UK*

ARTICLE INFO

Keywords:
Thermoelectric Oxide
Polycrystalline Strontium Titanate
Grain Boundary
Graphene Oxide
Carbon Black

ABSTRACT

Strontium titanate-based ceramics are promising n-type thermoelectrics due to their low cost and high thermal and chemical stability. Here, $SrTi_{0.85}Nb_{0.15}O_3$ was prepared with carbon additions of electrochemically produced graphene oxide (eGO) and commercially available carbon black (CB). Ceramic samples were sintered at 1700 K under a reducing atmosphere. XRD, HR-TEM and Raman spectra confirmed the matrix phase was cubic perovskite; there were no carbon residues. By incorporating graphene oxide, the electrical conductivity increased ninefold to 2818 S cm^{-1} at 300 K as a result of enhanced carrier mobility. In contrast, the carbon black samples exhibited low density and a small average grain size of ~1 μm. High-resolution X-ray photoelectron spectroscopy revealed the presence of a large number of ionised impurities in the carbon black samples, which significantly enhanced scattering effects; low thermal conductivities of 1.7 W m^{-1} K^{-1} were achieved at 873 K. The work reveals that eGO promotes charge transport in $SrTiO_3$, while CB significantly suppresses phonon transport. Both effects are relevant to the development of other thermoelectrics.

1. Introduction

Power generation by fossil energy is unsustainable and much energy is wasted in the form of heat. Alternative clean energy sources are required and thermoelectric (TE) technology offers many benefits through energy harvesting [1], since TE materials can convert heat to electricity without pollution [2]. The dimensionless thermoelectric figure-of-merit zT is commonly used to evaluate the TE conversion efficiency of a material,

$$zT = S^2 \sigma T / (\kappa_e + \kappa_l) \tag{1}$$

where S, σ, T, κ_e, κ_l refer to the Seebeck coefficient, electrical conductivity, the absolute temperature, electronic and lattice thermal conductivity, respectively. The quantity $S^2\sigma$ is denoted as the power factor, and the total thermal conductivity κ is the combination of κ_e and κ_l. For maximum TE efficiency, high electrical conductivity, a large Seebeck coefficient and low thermal conductivity are required, often embodied in the concept of a 'phonon-glass-electron-crystal (PGEC)' [2]. However, it is difficult to improve one TE parameter without compromising the others as the transport processes are linked, depending on the carrier concentration and the band structure [2,3]. Many commercially employed TE materials are based on tellurides such as PbTe and Bi_2Te_3 [1,4], the best of which can achieve $zT > 1$ from room temperature to 500 °C [5,6]. However, they contain rare, expensive and toxic elements and the materials degrade at high temperatures, restricting their use in waste heat recovery [1,7].

Over the last twenty years there has been growing interest in oxide TE materials (mainly layered cobalt oxides [8,9] and oxide perovskites [10]) because they are chemically and thermally stable at high temperatures and are cheaper, based on earth-abundant elements, and free of heavy elements [11,12]. Among the oxide TE materials, strontium titanate ($SrTiO_3$) is an attractive candidate as it has a band structure with flat bands close to the Fermi level which results in large electron effective mass and giant Seebeck coefficient values [12–14]. Pristine strontium titanate is an n-type, wide bandgap (3.2 eV) semiconductor with a cubic $Pm\bar{3}m$ perovskite structure [14,15]. Doping is an effective method to enhance carrier transport in $SrTiO_3$, and a high power factor of 3600 μW m^{-1} K^{-2} can be achieved at room temperature in La-doped

---

[*] Corresponding authors.
E-mail addresses: david.lewis-4@manchester.ac.uk (D.J. Lewis), robert.freer@manchester.ac.uk (R. Freer).

https://doi.org/10.1016/j.jallcom.2024.174242
Received 22 November 2023; Received in revised form 6 March 2024; Accepted 21 March 2024

single crystal $SrTiO_3$, comparable to that of Bi_2Te_3 [16]. However, pristine $SrTiO_3$ exhibits a high thermal conductivity (close to 10 W m^{-1} K^{-1} at room temperature) due to its simple crystal structure and the presence of light elements [17], which suppresses overall zT values. Nanostructuring strategies, such as nano-sized microstructures [1] and the use of nano-inclusions [14,18]; and fabricating composites [19], are widely employed to lower the thermal conductivity to ~ 4 W m^{-1} K^{-1} at room temperature [18]. By such efforts, polycrystalline strontium titanate generally yields maximum zT values at 0.3 but rarely exceeds 0.4 from room temperature to 1000 K [20–26].

Polycrystalline strontium titanate is cheaper and easier to fabricate into devices than single crystals [27–29]. However, the grain boundaries in polycrystalline strontium titanate reduce carrier transport [29]. Consequently, enhancing carrier transport in polycrystalline materials, in order that they approach the characteristics of single crystals, is a priority. Attention has focussed on the presence and role of double Schottky barriers formed in the grain boundary (GB) regions [30,31]. The barriers are generated by the depletion of positively charged oxygen vacancies and tend to scatter low energy carriers [32]. As a result, different grain boundary engineering strategies have been developed to reduce the resistance of the grain boundary regions [33]. Carbon-based materials such as graphene and graphene oxide, have been identified as excellent additives strontium titanate, acting as oxygen scavengers to improve the TE performance [26,34–40]. Lin *et al.* reported a single-crystal-like, electrical conductivity temperature dependence and an expanded operational window from room temperature to 1023 K in graphene incorporated La-doped $SrTiO_3$ [26]. It is believed the graphene/carbon acts as a reducing agent, consuming lattice oxygen, thereby reducing the height of the double Schottky barriers [29,40]. Subsequently, Cao *et al.* [35] and Ekren *et al.* [36] investigated the effects of different types of graphene and sintering atmospheres on A-site deficient La-doped $SrTiO_3$ and found that it was more effective to embed the samples in an oxygen scavenger (a mixture of 5% GnP and 95% of La-doped $SrTiO_3$) to minimise GB resistance. However, in Nb-doped $SrTiO_3$ Okhay *et al.*, reported that the addition of graphene oxide and the A-site deficiency play a more important role than an oxygen scavenger to increase carrier transport and produce single crystal like electrical conductivity [34]. Nevertheless, significantly enhanced electrical conductivity in polycrystalline strontium titanate, which sometimes is comparable to that in a single crystal, can be achieved without sacrificing the Seebeck coefficient to a large extent by introducing graphene/carbon as additives and/or oxygen scavengers [26,34–40]. Moreover, the use of graphene as a grain boundary additive can restrict grain growth and create extra scattering centres, thus limiting lattice thermal conductivity [26,34,36–40]. However, we do not have a comprehensive understanding of the role and behaviour of carbon/-Nb-$SrTiO_3$ formulations, and particularly the effects of different types of carbon additives. Additionally, other commercially available carbon species such as carbon black have been shown to be beneficial as an additive in oxide cobaltite [41], by simultaneously increasing electrical conductivity and suppressing thermal conductivity; nevertheless, carbon black has not been applied to thermoelectric $SrTiO_3$.

In this work, we investigated the effects of different types of carbon on the TE performances of $SrTi_{0.85}Nb_{0.15}O_3$. We introduced electrochemically produced graphene oxide (eGO) flakes (high C/O ratio) [42] and carbon black (CB) in the form of particles to strontium titanate. We have revealed that the incorporation of eGO leads to dense samples and high, single-crystal-like electrical conductivity as a function of temperature. In contrast, CB additions results in a low density, highly porous ceramics, but significantly reduces the thermal conductivity of $SrTiO_3$. This work highlights the effects of different types of carbon on the TE properties of strontium titanate, and provides guidance on the synthesis of metal oxides with different electrical and thermal properties.

2. Experimental methods

$SrTi_{0.85}Nb_{0.15}O_3$ (denoted as N15) powders were prepared *via* solid-state reaction with starting powders of $SrCO_3$, TiO_2 (both 99.9% grade from Sigma-Aldrich), and Nb_2O_5 (99.8%, PI-KEM). Sintering additives were TiO_2 (99.9%, Sigma-Aldrich), WO_3 (99.995%, Sigma-Aldrich) and V_2O_5 (99.6%, Sigma-Aldrich) [33]. The electrochemically produced graphene oxide (eGO, having a less disrupted conjugated structure, a higher carbon/oxygen ratio, and a less damaged graphitic structure than graphene oxide (GO) synthesised by the Hummers' method) was produced *via* a two-step electrochemical synthesis method [42]; the carbon black was obtained from Fisher Scientific (99.9+%, acetylene, 100% compressed). Graphene nanoplatelets (GnP, grade M25, from XG Sciences) were used in the sintering environment.

$SrCO_3$, TiO_2, and Nb_2O_5 were weighed according to the formulation of N15 and mixed with isopropanol (IPA) and zirconia milling balls (Retsch) with a mass ratio of 1:1:1. The mixtures were vibromilled for 24 h and dried at 363 K. The dried powders were calcined at 1473 K for 12 h in air, then mixed with sintering additives (2 wt% TiO_2, 1 wt% WO_3, and 0.5 wt% V_2O_5), tungsten carbide milling balls (Retsch), and IPA, and further milled in a planetary ball mill (PM100, Retsch) at 350 rpm for 4 h. For the eGO/N15 and CB/N15 composites, individual suspensions of as-prepared N15 powders, eGO, and CB with solvents of deionised water (DI water), or IPA were formed; all were individually tip sonicated (Sonics VCX 750 with a standard 0.5 in. diameter probe) for 0.5 h. Then the suspensions were mixed according to the required compositions and further sonicated for 0.5 h, then filtered and dried. The resulting powders were pressed uniaxially in steel dies into discs of 20 mm and 13 mm diameter at a pressure of 50 MPa. The compacts were buried in open alumina crucibles containing an oxygen scavenger (N15 powders with 5% GnP) and sintered at 1700 K for 24 hrs in a tube furnace with a 5% H_2/Ar atmosphere. The formulations with their sample codes are presented in Table 1.

Sample densities were determined *via* the Archimedes' method. Powder X-ray diffraction (XRD) analysis was carried out using a PANalytical X'Pert Pro with Cu Kα source with $2\theta = 20 - 100^\circ$. The XRD data were Rietveld-refined using TOPAS (Bruker AXS) software [43]. For scanning electron microscopy (SEM), the samples were ground, and then polished down to 0.04 μm with OPS colloid silica (MetPrep) and examined by Tescan Mira3 equipped with Energy-dispersive X-ray spectroscopy (EDX) and Electron Backscatter Diffraction (EBSD). The average grain sizes were determined via the linear intercept method as well as by EBSD. Carbon residue analyses employed a Horiba LabRAM Evolution HR 488 nm Raman Microscope; the data were processed by LabSpec6 software. X-ray photoelectron spectroscopy (XPS) was performed with a Kratos Axis Ultra with a monochromatic Al source; the pass energy was 20 eV for Core Level scans. Peak deconvolution employed CasaXPS software. The binding energy (BE) was charge-calibrated with respect to C 1 s spectrum located at BE = 284.8 eV. Transmission electron microscopy (TEM) samples were prepared by crushing; images were collected by FEI Titan G2 S/TEM.

Electrical conductivity and Seebeck coefficients were determined using an ULVAC ZEM-3 under a low-pressure He atmosphere (300 K – 873 K). Thermal conductivity was obtained from the relationship: $\kappa = \alpha\rho C_p$, where α is the thermal diffusivity, ρ is the bulk density, and C_p is

Table 1
The formulations investigated in this work and corresponding sample codes.

Formulation	Sample Code
N15	0 G
N15 + 0.2 wt% eGO	0.2 G
N15 + 0.6 wt% eGO	0.6 G
N15 + 1.0 wt% eGO	1.0 G
N15 + 1.0 wt% CB	1.0 C

the specific heat capacity. Thermal diffusivity α and the specific heat capacity C_p were determined from 300 K to 873 K in Ar using a Netzsch LFA-427, a Netzsch LFA-467 and a Netzsch STA 449 F3 Jupiter.

3. Results and discussions

SEM images of the CB, eGO, and N15 powders are presented in Figure S1 (Supplementary Material). The CB particles are agglomerated, several hundred nm in size, with individual grains several tens of nm in size. The eGO flakes have lateral sizes ~1.0 µm; the N15 powders are in the range of ~0.5 – 1.0 µm. Raman spectra were collected to determine carbon residues present in the samples after sintering (Figure S2). For CB and eGO, there are strong D band (around 1350 cm^{-1}) and G band (around 1600 cm^{-1}) intensities, with a low-intensity 2D band (around 2700 cm^{-1}), which are comparable to those reported for CB and graphene oxide (GO) [44]. However, there are no visible peaks in the Raman spectra of sintered 1.0 C and 1.0 G samples (Figure S2 and S3), suggesting there are no carbon residues. Samples densities are presented in Table 2; with the exception of 1.0 C (~ 84.8% dense) all samples were above 90% theoretical density.

XRD patterns of the samples are presented in Fig. 1(a) and confirm the $Pm\overline{3}m$ cubic perovskite as the dominant phase [45] with an absence of carbon peaks. For the samples containing eGO, *i.e.* 0.2 G, 0.6 G and 1.0 G, the perovskite peaks are displaced to lower angles with increasing amount of eGO, as indicated in Fig. 1(b). Whilst there is minimal difference between the lattice parameters for 0 G and 0.2 G, the peak shifting for the samples prepared with eGO is primarily attributed to the expansion of the lattice, driven by the formation of oxygen vacancies via the loss of lattice oxygen (Eq. 2). The lattice oxygen was converted to free oxygen, which can be further reduced by the eGO and increase the oxygen vacancy concentration during sintering at high temperatures > 1273 K [36,37,46].

$$O_O^\times \leftrightarrow V_O^{\cdot\cdot} + 2e^- + \frac{1}{2}O_2 \tag{2}$$

In contrast, the samples containing carbon black, 1.0 C, exhibit a higher perovskite peak position than the samples containing the same amount of eGO (*i.e.* 1.0 G) but still lower than the carbon-free samples (0 G). This indicates that the lattice parameter for 1.0 C is between that for 0 G and 1.0 G (Table 2), and is presumably related to the ability of eGO to generate more oxygen vacancies in $SrTiO_3$ than CB.

SEM images of the samples are shown in Fig. 2. There was no evidence of eGO, carbon black or carbon residues, in good agreement with the Raman results (Figures S2 and S3). The carbon-free samples (0 G) and all the samples containing eGO, *i.e.* 0.2 G, 0.6 G, and 1.0 C, are dense and exhibit polygonal-shaped grains with visible grain boundaries (Figs. 2(a) – 2(d)). In contrast the samples containing CB (1.0 C) are much more porous (Fig. 2(e)), consistent with the density data (Table 2). The average grain size of the samples (Table 2) varied from 9.5 µm in 0 G to 6.9 µm in 1.0 G (determined by the linear intercept method) and to 1.3 µm in 1.0 C (obtained from EBSD maps in Figure S4 as the grain boundaries are not visible in SEM images). Reduced grain sizes in strontium titanates prepared with graphene-based additions has previously been attributed to the presence of graphene at the GB restraining grain growth [26,34,37,38]. However, in this work, the eGO added to the strontium titanate is believed to be eliminated during the long sintering process at high temperature (Fig. 2 and Figures S2 and S3) [36], therefore the average grain size of samples ranging from 0 G to 1.0 G remain similar at the micron scale. In contrast, the average grain size of the 1.0 C samples was much smaller than that of 0 G samples, suggesting carbon black can act as a better grain growth inhibitor than eGO. The smaller grain size is favourable for achieving low thermal conductivity [47].

Table 2
Relative density, lattice parameter, and the average grain size of the samples.

Sample Code	Relative Density (%, ±0.4%)	Lattice Parameter (Å)*	Average Grain Size (µm)*
0 G	95.2	3.91708(6)	9.5(0.5)
0.2 G	93.7	3.91630(8)	9.2(0.4)
0.6 G	92.0	3.91962(6)	7.7(0.4)
1.0 G	90.5	3.92660(4)	6.9(0.3)
1.0 C	84.8	3.91870(6)	1.3(0.6)

* The uncertainties for the lattice parameters and average grain sizes are shown in brackets.

The SEM images also revealed multiple secondary phase (SP) precipitates in every sample (Fig. 2 and Figure S5) although they are difficult to identify in XRD patterns due to their low concentration. The small, white contrast precipitates are metallic tungsten and the larger, darker contrast precipitates are crystalline Ti-rich phases [33]. However, SEM-EDX analysis (Figure S6) showed that precipitates in the carbon-free samples (0 G, Figure S6(a)) are enriched in Ti and Nb, but deficient in Sr, suggesting they are niobium titanate-based materials [33,48]. In samples containing eGO, for example, 1.0 G (Figure S6(b)), the distributions of Ti and Sr in the precipitates are similar to that in 0 G, but are deficient in Nb. This can be explained by the reduction of Ti^{4+} in the secondary phase (where it is TiO_2-based) to Ti^{3+} (which is Ti_2O_3-based). In the Ti^{3+}-rich precipitates the solubility of Nb is significantly lower in than in the Ti^{4+}-rich precipitates [33]. In contrast, for the samples containing CB, (1.0 C), the precipitates are much less porous than the matrix phase (Figure S5). The Sr concentration is higher and the Ti concentration lower in the precipitates than in the matrix of 1.0 C samples (Figure S6(c)).

Since all samples exhibit a cubic perovskite structure, we have selected 0.2 G as a representative for high resolution, high-angle annular dark-field scanning transmission electron microscopy (HAADF-STEM) analysis; the data are presented in Figure S7. The TEM analysis confirmed the existence of a cubic perovskite structure with identical interplanar spacing of 4.0 Å for (010) planes. In addition, the selected area shows no trace of defects, suggesting eGO did not significantly affect the primary grain structures.

XPS analysis revealed the valence states of the constituent elements Ti and Nb in 0 G, 1.0 G, and 1.0 C samples (Fig. 3). The Ti 2p orbitals split into Ti $2p_{1/2}$ and Ti $2p_{3/2}$ core levels with a spin orbital splitting energy of ~5.7 eV; the Nb 3d orbitals contain Nb $3d_{5/2}$ and Nb $3d_{3/2}$ core levels with a spin orbital splitting energy of ~2.7 eV; both are consistent with earlier studies [25,49]. The Ti peaks in 1.0 C samples are less symmetric than the peaks in 0 G and 1.0 G samples. The fitting result further indicates the presence of Ti^{4+}, Ti^{3+}, as well as Ti^{2+} states in 1.0 C samples while only Ti^{4+} and Ti^{3+} states were identified in 0 G and 1.0 G samples. The binding energy of Ti^{4+}, Ti^{3+}, and Ti^{2+} states (Table S1) match the previously reported Ti 2p energy data [50,51]. Moreover, the concentrations of Ti^{3+} ($[Ti^{3+}]$) are comparable at 2% in 0 G and 1.0 G, while 1.0 C contains 6% of $[Ti^{3+}]$ as well as 3% $[Ti^{2+}]$. For the Nb 3d orbitals, only two peaks are observed in 0 G and 1.0 G samples, while more peaks are found in 1.0 C samples. The fitting results reveal that 0 G and 1.0 G exhibit only Nb^{5+} states, while Nb^{5+}, as well as high concentrations of Nb^{4+} and Nb^{2+} states were found in 1.0 C. Again the binding energy of Nb^{5+}, Nb^{4+}, and Nb^{2+} states (Table S1) are comparable to earlier reported Nb 3d energy data [49,52]. The high concentrations of the low Ti and Nb states are responsible for intensive ionised impurity scattering, which can potentially lead to low carrier transport [53].

The charge transport characteristics of the samples are presented in Fig. 4. Starting with samples containing eGO (Fig. 4(a) – (c)) it is clear they exhibit much higher electrical conductivity than 0 G samples and show single-crystal-like temperature dependences from 300 K – 873 K (Fig. 4(a)). On the other hand, the 0 G samples exhibit a peak, with maximum electrical conductivity at 523 K. Near room temperature (300 K) electrical conductivity increased from 327 S cm^{-1} in 0 G to 2818 S cm^{-1} in 1.0 G. A similar change was observed in related graphene oxide/N15 work (dashed and solid line in Fig. 4(a)) [34], where

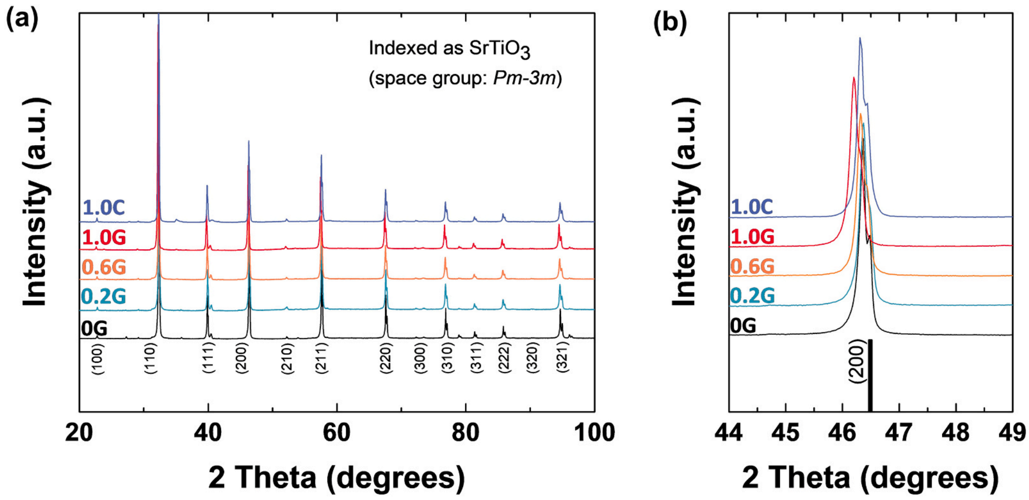

Fig. 1. XRD patterns for the samples: (a) 2θ from 20° to 100° with the standard $SrTiO_3$ pattern [45]; (b) enlarged pattern from 2θ from 44° to 49° showing details of the (200) peak. There is no evidence of any secondary phase. In Fig. 1(b) there is a clear displacement of the peaks to the left with increasing eGO content.

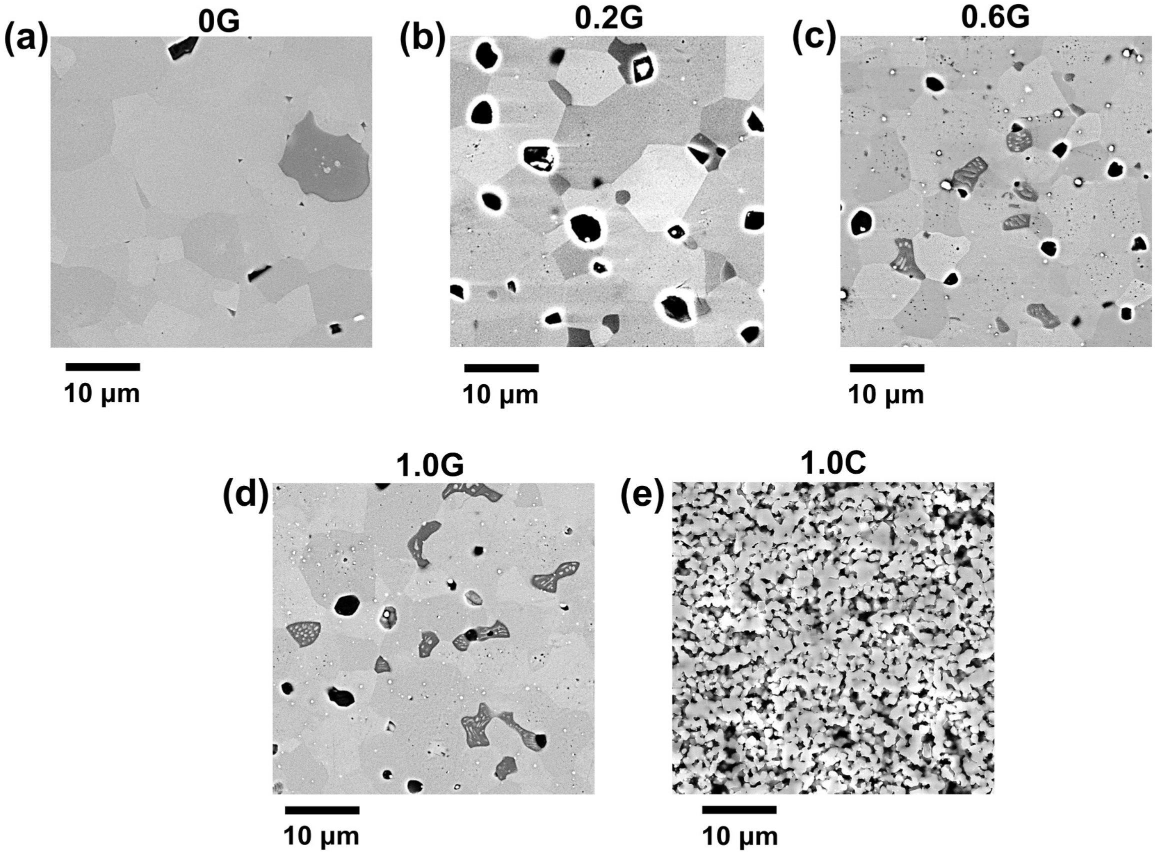

Fig. 2. SEM images of polished sample surfaces. The grain structure of 1.0 C was revealed *via* the EBSD maps (Fig. S4). In images (b), (c) and (d) the dark precipitates are Ti-rich phases and the small white precipitates are metallic tungsten (added as sintering aid). With increasing eGO content of the grain size of the samples reduces (details in Table 2).

graphene oxide (GO) produced by the Hummers-based method was incorporated in A-site deficient $Sr_{0.98}Ti_{0.85}Nb_{0.15}O_3$ (denote as n15). However, the rate of increase of electrical conductivity in the reported work GO/N15 work is smaller than with eGO here, although electrical conductivity values are comparable at $T > 600$ K [34]. This can be explained by the higher carbon/oxygen ratio in the eGO than in the GO produced by the Hummers-based method [42]; a higher carbon content will enable greater consumption of oxygen during the synthesis process, thereby enhancing the carrier (electron) concentration according to Eq. 2.

The Seebeck coefficients for the samples containing eGO (Fig. 4(b)) are negative confirming n-type conduction. The absolute Seebeck coefficients increased with temperature but decreased when eGO was introduced. For 0 G samples, the Seebeck coefficients vary from −93 μV K^{-1} at 300 K to −188 μV K^{-1} at 873 K, with marginally lower values for 0.2 G, 0.6 G and 1.0 G (~ −70 μV K^{-1} at 300 K to ~ −145 μV K^{-1}at

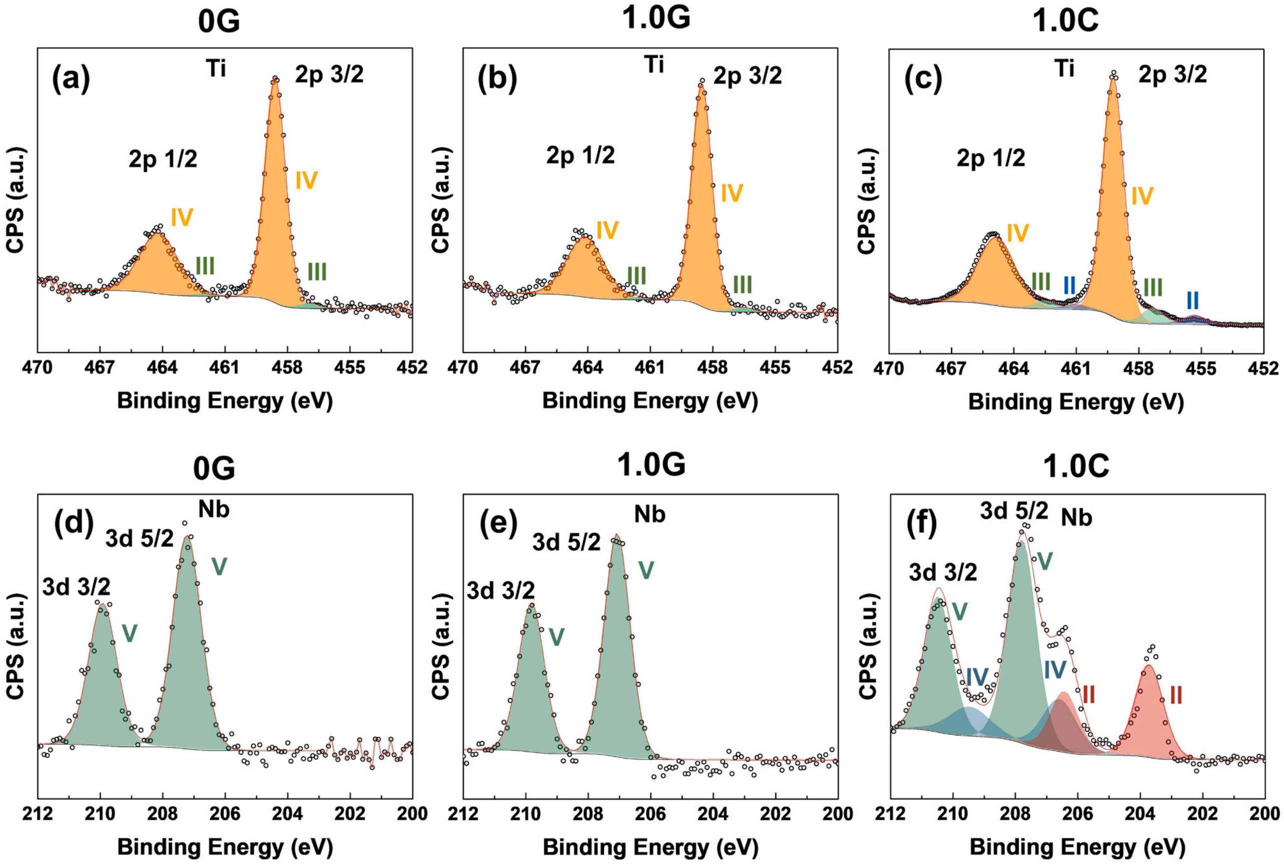

Fig. 3. XPS analysis of 0 G, 1.0 G, and 1.0 C samples: (a) – (c) Ti 2p orbitals; (d) – (f) Nb 3d orbitals. Detailed descriptions and discussion of the data are provided in the accompanying text.

873 K). The Seebeck coefficient is related to the carrier concentration through the relationship shown in Eq. 3:

$$S = \frac{C_e}{n} + \frac{\pi^2 k_B^2 T}{3e}\left[\frac{\partial \ln \mu(\varepsilon)}{\partial \varepsilon}\right]_{\varepsilon=\varepsilon_F} \tag{3}$$

where S, C_e, n, $\mu(\varepsilon)$ refer to the Seebeck Coefficient, electronic specific heat, carrier concentration, and energy correlated carrier mobility, respectively. In many cases Eq. 3 can be simplified to just the first term, *i. e.* $S \approx \frac{C_e}{n}$ [54]. Therefore, the larger Seebeck coefficients for the eGO-free samples, compared to the samples containing eGO, can be explained by the lower carrier concentration, consistent with the changes of electrical conductivity outlined above. The greater reduction of Seebeck coefficient from 0 G to 1.0 G, compared to the earlier graphene oxide/N15 work [34], suggests a higher change in the carrier concentration in the present work.

The power factor values as a function of temperature (Fig. 4(c)) are lowest for 0 G samples, with a minimum at 300 K (285 μW m^{-1} K^{-2}) and a peak at 1132 μW m^{-1} K^{-2} at 723 K. For samples containing eGO there is less variation in power factor with temperature; 0.6 G exhibits the highest value of 1659 μW m^{-1} K^{-2} at 323 K. Additionally, the power factors for 0.6 G and 1 G remain high (> 1500 μW $m^{-1}K^{-2}$) from 323 K to 473 K, reflecting significantly improved thermoelectric performance for strontium titanate at lower temperatures [25,55].

Fig. 4(d) – (f) present the equivalent charge transport properties of the CB samples (1.0 C) compared to the carbon-free samples (0 G) and the eGO samples with the maximum additive level (1.0 G). The electrical conductivity of 1.0 C (Fig. 4(d)) shows thermally activated carrier behaviour from 323 K to 873 K, which is the opposite to that for 1.0 G, and indeed the conductivity of 1.0 C is several orders of magnitude lower, reaching 0.19 S cm^{-1} at 323 K and 4.3 S cm^{-1} at 873 K. The low electrical conductivity for 1.0 C samples is unusual as CB is widely used to enhance electrical conductivity of battery and other materials (*e.g.* $Ca_3Co_4O_9$ [41], $LiMn_2O_4$ [56], MnO_x [57], SnSe [58]). However, the matrix materials of these CB composites generally exhibit low electrical conductivity at room temperature (< 1 S cm^{-1}) and thermally activated carrier behaviour [41,56,58]. On the other hand, the Seebeck coefficients for 1.0 C are between those of 0 G and 1.0 G (Fig. 4(e)), reaching −83 μV K^{-1} at 323 K and −167 μV K^{-1} at 873 K. This suggests for 1.0 C, that the carrier concentration and oxygen vacancy level at fixed temperature are between those for 0 G and 1.0 G, (according to Eqs. 2 and 3) which is consistent with the lattice parameter trends. Consequently, the power factor values for 1.0 C are the lowest among all the samples, ranging from 0.13 μW m^{-1} K^{-2} at 323 K to 12 μW m^{-1} K^{-2} at 873 K (Fig. 4(f)).

To further understand the effect of eGO and CB on the charge transport properties of $SrTi_{0.85}Nb_{0.15}O_3$ (*i.e.* N15), the carrier concentration and carrier mobility were calculated from the modified Heikes' formula (Equations S1 and S2). For the eGO samples, the calculated carrier concentration at room temperature increased by 20% from 4.1 × 10^{21} cm^{-3} in 0 G to 4.9 × 10^{21} cm^{-3} in 1.0 G (Figure S8), whilst the carrier mobility increased by 7 times, from 0.5 cm^2 V^{-1} s^{-1} in 0 G to 3.4 cm^2 V^{-1} s^{-1} in 1.0 G (Figure S8). However, the carrier mobility for 1.0 C samples is too low to be meaningful (0.0 cm^2 V^{-1} s^{-1}, Table S2). The weighted mobility μ_w can give mobility information *via* a different approach, and is particularly useful for low mobility materials at high temperatures (T > 300 K) [59]. Therefore, the weighted mobility μ_w as a function of temperature, as well as the electron effective mass m^* (in terms of m^*/m_e, m_e is the electron mass) were calculated *via* Equations S3 and S4; results are presented in Figure S9 and Table S2. There is very little variation in the effective mass (Table S2); since the effective mass reflects the electronic band structure of the materials [60], the similarity

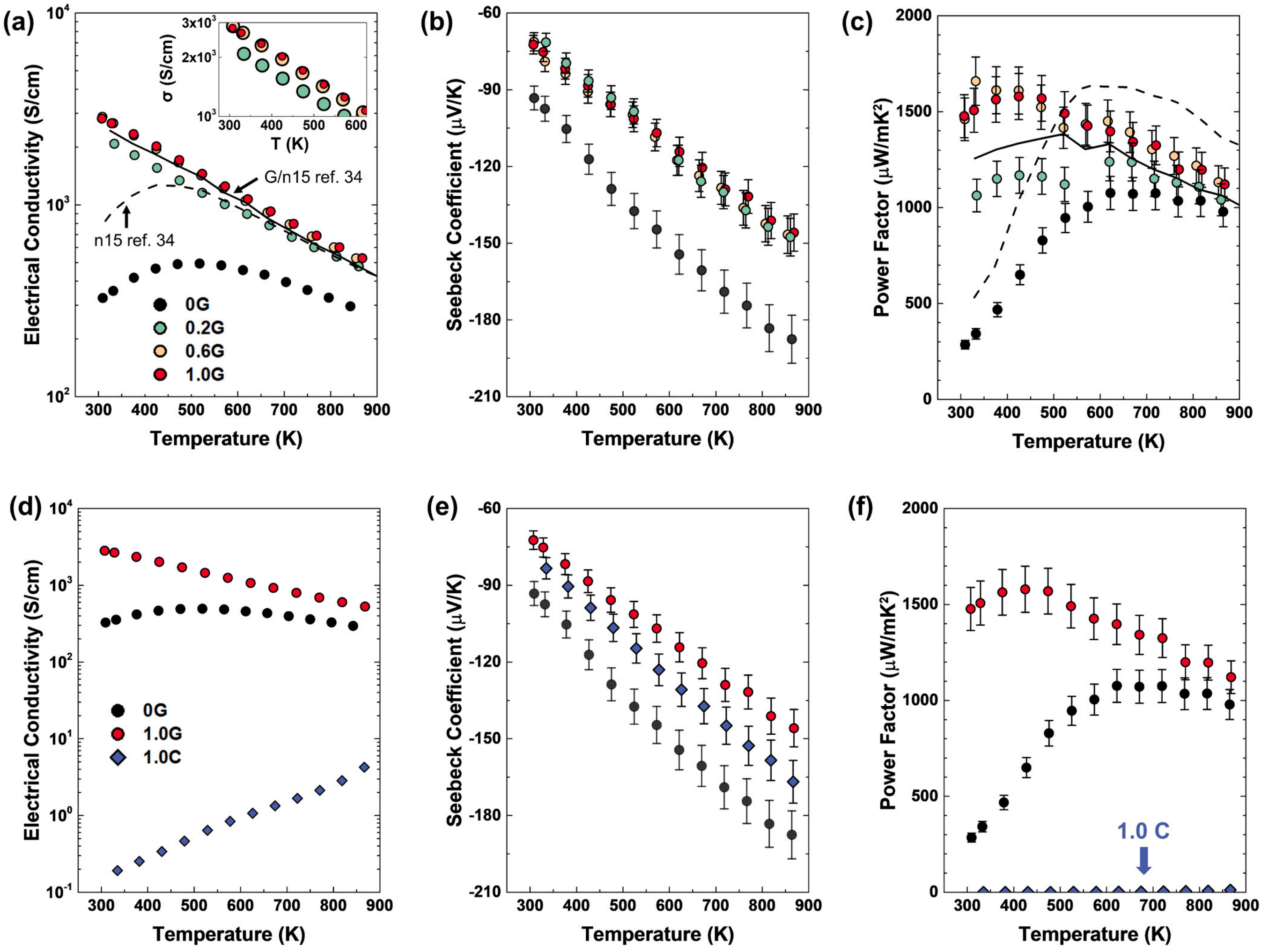

Fig. 4. Charge transport properties for samples containing eGO as a function of temperature: (a) electrical conductivity, the inserted figure shows the comparable data for 0.6 G and 1.0 G; (b) Seebeck coefficient; (c) power factor. The dashed and solid lines are taken from the work of Okhay *et al.*, n15 refers to $Sr_{0.98}Ti_{0.85}Nb_{0.15}O_3$ and G represents graphene oxide produced by the Hummers method [34]. Parts (d,e,f) show charge transport properties for 0 G, 1.0 G and 1.0 C: (d) electrical conductivity; (e) the Seebeck coefficient; (f) power factor.

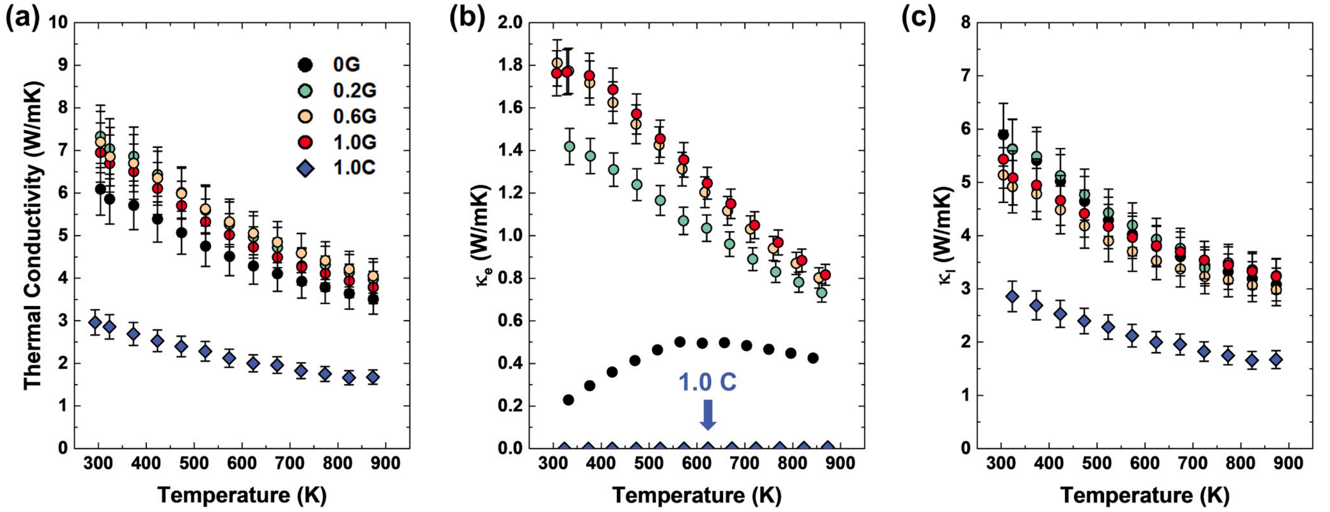

Fig. 5. Thermal properties of samples as a function of temperature: (a) Total thermal conductivity; (b) Electronic thermal conductivity; (c) Lattice thermal conductivity. The samples prepared with carbon black additions (1.0 C) exhibit exceptionally low thermal conductivities.

of the m^* values suggest the perovskite N15 phase is not significantly affected by the carbon additives.

Data for the weighted mobility (μ_w) as a function of temperature are very similar in terms of trends to the original mobility data and electrical conductivity (Fig. 4 and Figure S8), indicating both eGO and CB have a significant impact on carrier mobility. At 300 K the samples containing eGO have the highest μ_w (~290 cm^2 V^{-1} s^{-1}), followed by the 0 G samples (~40 cm^2 V^{-1} s^{-1}), while the samples with CB have the lowest μ_w (0.02 cm^2 V^{-1} s^{-1}). With increasing temperature, the μ_w of samples containing eGO decreased at $T^{-3/2}$, suggesting phonon scattering of carriers is dominant and grain boundary scattering, which occurs in the carbon-free samples (0 G), is negligible [59,61,62]. The μ_w of 1.0 C samples increased monotonically with temperature, suggesting that scattering from defects, such as boundaries, voids (supported by SEM and EBSD results in Fig. 2 and S4) and ionised impurities (supported by XPS results in Fig. 3), is dominant [53,59]. Therefore, it is concluded that eGO can promote electrical conductivity in SrTiO$_3$ by reducing the grain boundary effect [29]; while in contrast, CB particles increase the concentration of voids and defects. The latter is potentially related to the tendency of CB to build agglomerated networks [63,64]. Such networks can concentrate local strain [63], pin grain boundaries, which together with inhomogeneous agglomerations lead to poor carrier mobility.

The thermal transport characteristics are presented in Fig. 5; the experimentally-determined thermal diffusivity, heat capacity, and the Lorenz number as a function of temperature are shown in Figure S10. All the samples containing eGO (0.2 G, 0.6 G, and 1.0 G) have comparable and high thermal diffusivities (Figure S10(a)) of 2.8 mm^2 s^{-1} at 300 K to 1.3 mm^2 s^{-1} at 873 K, whilst the 0 G samples have modest thermal diffusivity values (1.1 – 2.3 mm^2 s^{-1}) and the 1.0 C samples the lowest ones (0.7 – 1.6 mm^2 s^{-1}). The heat capacity C_p of 1.0 C is ~20% less than that for SrTiO$_3$-based ceramics (Figure S10(b), 0.5 J g^{-1} K^{-1} for 1.0 C at 873 K compared to 0.62 J g^{-1} K^{-1} for SrTi$_{0.85}$Nb$_{0.15}$O$_3$ [33]). The low C_p in 1.0 C is attributed to: (i) the high porosity, (ii) the reduced C_p from acoustic phonons (potentially related to weakened ionic bonding in 1.0 C from high concentrations of low valence states Ti and Nb) [65], and (iii) Sr-rich secondary phases in 1.0 C (Figure S6). Indeed, high Sr content and low Ti content can generally lower C_p in SrTiO$_3$-based materials (*e.g.* C_p of Sr$_2$TiO$_4$ and SrO are smaller than that of SrTiO$_3$) [33,65–67].

The total thermal conductivity κ is shown in Fig. 5(a); all the samples exhibit similar temperature dependencies. The samples containing eGO exhibit the highest thermal conductivity, ranging from 7.3 W m^{-1} K^{-1} at 300 K to 4 W m^{-1} K^{-1} at 873 K. This is 15% higher than for the 0 G samples (3.5 – 6.2 W m^{-1} K^{-1}). The 1.0 C samples exhibit the lowest thermal conductivity of 1.7 – 2.9 W m^{-1} K^{-1} as a consequence of the low density, low thermal diffusivity, and low heat capacity. These values represent the lowest thermal conductivities reported for SrTiO$_3$-based ceramics [47,68].

The electronic thermal conductivity κ_e can be determined *via* the Wiedemann–Franz law: $\kappa_e = L\sigma T$, and is shown in Fig. 5(b); the Lorenz number L is obtained from the Seebeck coefficients (Figure S10(c)) [69]. The lattice thermal conductivity, deduced from $\kappa_l = \kappa - \kappa_e$, is shown in Fig. 5(c). The κ_e values for 0.2 G, 0.6 G and 1.0 G are high, up to 2 W m^{-1} K^{-1} at 300 K as a result of the high electrical conductivity, thereby contributing 25% of the total thermal conductivity. For 0 G samples, the κ_e values are modest at 0.2 – 0.5 W m^{-1} K^{-1}, and for 1.0 C samples, the κ_e is exceptionally low, less than 0.01 W m^{-1} K^{-1}.

The lattice thermal conductivities κ_l (Fig. 5c) for 0 G to 1.0 G are comparable and differ only in the uncertainty in the measurements (~ 3.0 – 5.5 W m^{-1} K^{-1}), while the κ_l of 1.0 C samples is 50% lower (1.7 – 2.9 W m^{-1} K^{-1}). The κ_l is related to the sound velocity v_s, the phonon mean free path l, and the phonon relaxation timeτ, through the Debye-Callaway model [70]:

$$\kappa_l = \frac{1}{3}C_v v_s l = \frac{1}{3}C_v v_s^2 \tau \tag{6}$$

where C_v is the volume heat capacity. The first two terms in Eq. 6 are insensitive to temperature and structural changes [71,72], while the phonon mean free path and the phonon relaxation time can be affected by the various scattering processes. Moreover, the phonon relaxation timeτ is related to phonon–phonon scattering (τ_{phonon}), point defect scattering (τ_{defect}), and boundary scattering ($\tau_{boundary}$) [70]:

$$\tau^{-1} = \tau_{phonon}^{-1} + \tau_{defect}^{-1} + \tau_{boundary}^{-1} \tag{7}$$

The similarity of lattice thermal conductivities for samples containing eGO, (*i.e.* 0.2 G, 0.6 G, and 1.0 G) and the 0 G samples suggests that comparable phonon-phonon scattering operates in all these samples, which have similar grain sizes, similar densities, and almost identical [Ti^{3+}] contents. It is noted that point defect scattering, caused by the oxygen vacancies, has a minimal contribution to lattice thermal conductivity, presumably because modification to the samples eGO only affected the grain boundary regions and not the matrix phase. For 1.0 C samples, the significantly lowered lattice thermal conductivity can be attributed to enhanced point defect scattering (high concentrations of [Ti^{3+}], [Nb^{4+}], and [Nb^{2+}] were determined by XPS, Fig. 3) and enhanced boundary scattering from the significantly reduced average grain size (from 9.5 µm to 1.3 µm, Table 2), and increased porosity (Fig. 2).

The thermoelectric figure-of-merit zT (Fig. 6) increased with temperature, with the highest value of 0.26 at 873 K for 0.6 G samples. Overall, the zT of SrTi$_{0.85}$Nb$_{0.15}$O$_3$ has been significantly improved at low temperatures (300 K – 500 K) by the presence of eGO, primarily as a result of the enhanced electrical conductivity and power factor. In fact the power factor is the highest among all documented graphene/SrTi$_{0.85}$Nb$_{0.15}$O$_3$ at 323 K (Fig. 7(a)). The high power factor and electrical conductivity are essential for high power output and low energy loss in TE devices; therefore, eGO extends the operational window of SrTiO$_3$ to room temperatures. On the other hand, the samples containing CB exhibited exceptionally low thermal conductivity for SrTiO$_3$, approximately half that for typical graphene/SrTiO$_3$ systems (Fig. 7(b)). Thus, we have achieved both high electrical conductivity SrTiO$_3$ and low thermal conductivity SrTiO$_3$ *via* a simple processing route with carbon as additives. These results provide the basis for future investigations to maximise the TE performance of strontium titanate through the use of different carbon additives. We have shown the importance of controlling the defect levels in CB/SrTiO$_3$, the combined effects of CB and eGO in SrTiO$_3$, and optimising CB and eGO level to

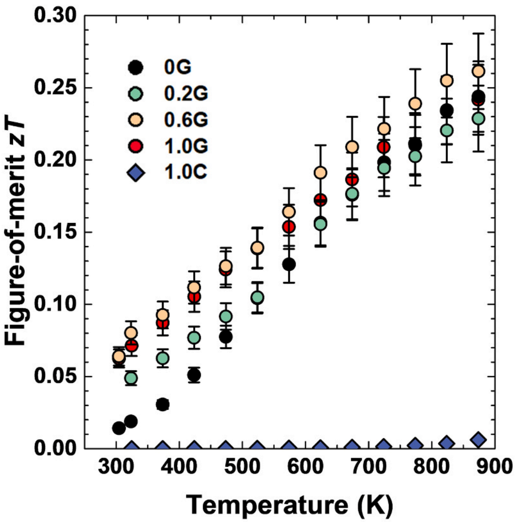

Fig. 6. Thermoelectric figure-of-merit zT values of all samples as a function of temperature. The highest zT values of 0.26 at 873 K were achieved in the 0.6 wt % eGO/SrTi$_{0.85}$Nb$_{0.15}$O$_3$ samples.

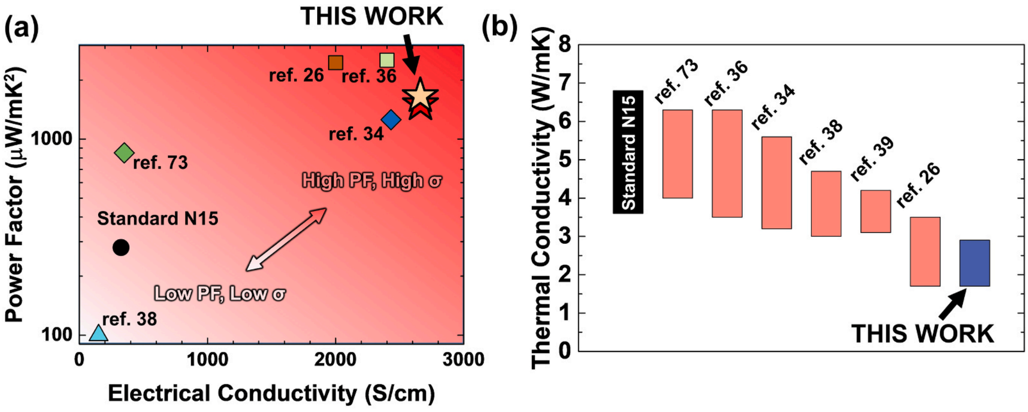

Fig. 7. Comparison of TE properties for $SrTiO_3$-composites in this work with reported data for typical graphene/donor-doped-$SrTiO_3$ [26,34,36,38,39,73]. (a) Electrical conductivity and power factor at 323 K. 'This Work' data is for eGO-added sample (1.0 G). Note that data points in the shapes of diamonds, triangles and squares represent the matrix materials of N15 ($SrTi_{0.85}Nb_{0.15}O_3$), other Nb-doped $SrTiO_3$, and La-doped $SrTiO_3$, respectively; (b) Thermal conductivity from 300 K – 800 K; 'This Work' data is for CB sample, highlighting the value of CB for reducing thermal conductivity.

achieve the highest zT in $SrTiO_3$.

4. Conclusions

Good quality polycrystalline $SrTi_{0.85}Nb_{0.15}O_3$ samples containing additions of graphene oxide and carbon black were prepared by solid state reaction route. The matrix phase is cubic perovskite with a small amount of second phase; there was no evidence of carbon or carbon residues. The product densities decreased slightly with eGO additions and significantly reduced with CB additions. Grain growth of the matrix was marginally impeded by eGO additions, but significantly constrained by CB additions. Further, the CB tended to agglomerate leading to second phase precipitates and higher levels of porosity. XPS revealed the presence of high concentrations of low valence state ionised impurities of Ti^{2+}, Ti^{3+} and Nb^{2+}, Nb^{4+} ions in CB/$SrTi_{0.85}Nb_{0.15}O_3$ samples, while there was a trace of Ti^{3+} in eGO/$SrTi_{0.85}Nb_{0.15}O_3$. The presence of ionised impurities can enhance the scattering of both charge carriers and phonons. Importantly, HR-TEM analysis and weighted mobility analysis indicate that additions of eGO and CB have negligible impact on the crystal structure and electronic band structure of the matrix strontium titanate phase, suggesting that these carbon additives mainly affected the grain boundary regions.

The electrical conductivity of eGO/$SrTi_{0.85}Nb_{0.15}O_3$ was significantly higher than that of $SrTi_{0.85}Nb_{0.15}O_3$ (2818 S cm^{-1} compared to 327 S cm^{-1}at 300 K), as a result of a reduced grain boundary barrier and enhanced carrier mobility; this led to high power factors, greater than 1500 μW mK^{-2} at 323 K – 473 K. In CB/$SrTi_{0.85}Nb_{0.15}O_3$, there was evidence of significantly enhanced phonon scattering; addition of 1.0 wt % carbon black appeared to promote the formation of grain boundaries, defects, and voids in $SrTiO_3$. As a result, an exceptionally low thermal conductivity of 1.7 W m^{-1} K^{-1} was achieved at 873 K in 1.0 wt% CB/$SrTi_{0.85}Nb_{0.15}O_3$. The highest zT values were 0.26 at 873 K in the 0.6 wt % eGO/$SrTi_{0.85}Nb_{0.15}O_3$ samples. This study demonstrates an effective approach to control the microstructure, electrical and thermal properties of strontium titanate. The charge transport properties were significantly enhanced by eGO additions, whilst thermal conductivity and density were effectively reduced by CB additions.

CRediT authorship contribution statement

Jianyun Cao: Resources, Methodology, Conceptualization. **Xiaodong Liu:** Investigation, Formal analysis. **Stephanie R Mudd:** Investigation, Formal analysis. **David J Lewis:** Writing – review & editing, Validation, Supervision, Resources, Project administration, Methodology, Funding acquisition, Conceptualization. **Robert Freer:** Writing – review & editing, Visualization, Supervision, Resources, Project administration, Funding acquisition, Conceptualization. **Yibing Zhu:** Writing – original draft, Visualization, Validation, Methodology, Investigation, Formal analysis, Data curation. **Dursun Ekren:** Resources, Methodology, Conceptualization. **Rebecca Boston:** Investigation, Formal analysis. **Xiuqi Xia:** Investigation. **Yi Li:** Investigation, Formal analysis. **Ian A Kinloch:** Resources.

Declaration of Competing Interest

The authors declare that they have no known competing financial interests or personal relationships that could have appeared to influence the work reported in this paper

Data availability

Data are available within the manuscript

Acknowledgements

The authors are grateful to the EPSRC for the provision of funding for this work (EP/H043462, EP/I036230/1, EP/ L014068/1, and EP/ L017695/1 acknowledged by R.F.; DJL acknowledges EP/R022518/1); The work was also supported by the Henry Royce Institute for Advanced Materials, funded through EPSRC Grants EP/R00661X/1, EP/S019367/1, EP/P025021/1, and EP/ P025498/1. We gratefully acknowledge the support from X-Ray staff and use of facilities in the Department of Materials in the University of Manchester. All research data supporting this work are directly available within this publication.

Supplementary material

Additional SEM images, EDS and EBSD maps, Raman spectra, XPS binding energies, TEM images, and additional thermoelectric transport properties.

Appendix A. Supporting information

Supplementary data associated with this article can be found in the online version at doi:10.1016/j.jallcom.2024.174242.

References

[1] K. Koumoto, Y. Wang, R. Zhang, A. Kosuga, R. Funahashi, Oxide thermoelectric materials: a nanostructuring approach, Annu Rev. Mater. Res. 40 (2010) 363–394.

[2] G.J. Snyder, E.S. Toberer, Complex thermoelectric materials, Nat. Mater. 7 (2) (2008) 105–114.

[3] M.H. Elsheikh, D.A. Shnawah, M.F.M. Sabri, S.B.M. Said, M.H. Hassan, M.B. A. Bashir, M. Mohamad, A review on thermoelectric renewable energy: principle parameters that affect their performance, Renew. Sustain. Energy Rev. 30 (2014) 337–355.

[4] D. Zhao, G. Tan, A review of thermoelectric cooling: materials, modeling and applications, Appl. Therm. Eng. 66 (1-2) (2014) 15–24.

[5] H. Liu, Q. Sun, Y. Zhong, Q. Deng, L. Gan, F. Lv, X. Shi, Z. Chen, R. Ang, High-performance in n-type PbTe-based thermoelectric materials achieved by synergistically dynamic doping and energy filtering, Nano Energy 91 (2022) 106701–106709, 106706.

[6] S.I. Kim, K.H. Lee, H.A. Mun, H.S. Kim, S.W. Hwang, J.W. Roh, D.J. Yang, W. H. Shin, X.S. Li, Y.H. Lee, Dense dislocation arrays embedded in grain boundaries for high-performance bulk thermoelectrics, Science 348 (6230) (2015) 109–114.

[7] H. Ohta, S. Kim, Y. Mune, T. Mizoguchi, K. Nomura, S. Ohta, T. Nomura, Y. Nakanishi, Y. Ikuhara, M. Hirano, Giant thermoelectric Seebeck coefficient of a two-dimensional electron gas in $SrTiO_3$, Nat. Mater. 6 (2) (2007) 129–134.

[8] Y. Takashima, Y.-q Zhang, J. Wei, B. Feng, Y. Ikuhara, H.J. Cho, H. Ohta, Layered cobalt oxide epitaxial films exhibiting thermoelectric ZT= 0.11 at room temperature, J. Mater. Chem. A 9 (1) (2021) 274–280.

[9] X. Zhang, Y. Zhang, L. Wu, A. Tsuruta, M. Mikami, H.J. Cho, H. Ohta, Ba1/3CoO2: A Thermoelectric Oxide Showing a Reliable ZT of~ 0.55 at 600° C in Air, ACS Appl. Mater. Interfaces 14 (29) (2022) 33355–33360.

[10] Y. Zheng, M. Zou, W. Zhang, D. Yi, J. Lan, C.-W. Nan, Y.-H. Lin, Electrical and thermal transport behaviours of high-entropy perovskite thermoelectric oxides, J. Adv. Ceram. 10 (2021) 377–384.

[11] H. Ohta, Thermoelectrics based on strontium titanate, Mater. Today 10 (10) (2007) 44–49.

[12] Y. Yin, B. Tudu, A. Tiwari, Recent advances in oxide thermoelectric materials and modules, Vacuum 146 (2017) 356–374.

[13] H. Ohta, K. Sugiura, K. Koumoto, Recent progress in oxide thermoelectric materials: p-type $Ca_3Co_4O_9$ and n-type $SrTiO_3$, Inorg. Chem. 47 (19) (2008) 8429–8436.

[14] F. Azough, A. Gholinia, D.T. Alvarez-Ruiz, E. Duran, D.M. Kepaptsoglou, A. S. Eggeman, Q.M. Ramasse, R. Freer, Self-nanostructuring in $SrTiO_3$: a novel strategy for enhancement of thermoelectric response in oxides, ACS Appl. Mater. Interfaces 11 (36) (2019) 32833–32843.

[15] T.K. Townsend, N.D. Browning, F.E. Osterloh, Nanoscale strontium titanate photocatalysts for overall water splitting, ACS Nano 6 (8) (2012) 7420–7426.

[16] T. Okuda, K. Nakanishi, S. Miyasaka, Y. Tokura, Large thermoelectric response of metallic perovskites: $Sr_{1-x}La_xTiO_3$ ($0< \sim x< \sim 0.1$), Phys. Rev. B 63 (11) (2001) 113104–113107.

[17] M. Ohtaki, Recent aspects of oxide thermoelectric materials for power generation from mid-to-high temperature heat source, J. Ceram. Soc. Jpn 119 (1395) (2011) 770–775.

[18] N. Wang, H. Chen, H. He, W. Norimatsu, M. Kusunoki, K. Koumoto, Enhanced thermoelectric performance of Nb-doped $SrTiO_3$ by nano-inclusion with low thermal conductivity, Sci. Rep. 3 (1) (2013) 3449, 3441-3445.

[19] J. Huang, Y. Liu, P. Yan, J. Gao, Y. Fan, W. Jiang, Mechanically exfoliated MoS2 nanoflakes for optimizing the thermoelectric performance of SrTiO3-based ceramic composites, J. Mater. 8 (4) (2022) 790–798.

[20] A. Kovalevsky, A. Yaremchenko, S. Populoh, P. Thiel, D. Fagg, A. Weidenkaff, J. Frade, Towards a high thermoelectric performance in rare-earth substituted $SrTiO_3$: effects provided by strongly-reducing sintering conditions, Phys. Chem. Chem. Phys. 16 (48) (2014) 26946–26954.

[21] A. Tkach, Jo Resende, K.V. Saravanan, M.E. Costa, P. Diaz-Chao, E. Guilmeau, O. Okhay, P.M. Vilarinho, Abnormal grain growth as a method to enhance the thermoelectric performance of Nb-doped strontium titanate ceramics, ACS Sustain. Chem. Eng. 6 (12) (2018) 15988–15994.

[22] K. Park, J.S. Son, S.I. Woo, K. Shin, M.W. Oh, S.D. Park, T. Hyeon, Colloidal synthesis and thermoelectric properties of La-doped $SrTiO_3$ nanoparticles, J. Mater. Chem. A 2 (12) (2014) 4217–4224.

[23] J. Wang, B. Zhang, H. Kang, Y. Li, X. Yaer, J. Li, Q. Tan, S. Zhang, G. Fan, C. Liu, Record high thermoelectric performance in bulk $SrTiO_3$ via nano-scale modulation doping, Nano Energy 35 (2017) 387–395.

[24] J. Li, J. Wang, J. Li, Y. Li, H. Yang, H. Yu, X. Ma, X. Yaer, L. Liu, L. Miao, Broadening the temperature range for high thermoelectric performance of bulk polycrystalline strontium titanate by controlling the electronic transport properties, J. Mater. Chem. C. 6 (28) (2018) 7594–7603.

[25] D. Ekren, F. Azough, A. Gholinia, S.J. Day, D. Hernandez-Maldonado, D. M. Kepaptsoglou, Q.M. Ramasse, R. Freer, Enhancing the thermoelectric power factor of $Sr_{0.9}Nd_{0.1}TiO_3$ through control of the nanostructure and microstructure, J. Mater. Chem. A 6 (48) (2018) 24928–24939.

[26] Y. Lin, C. Norman, D. Srivastava, F. Azough, L. Wang, M. Robbins, K. Simpson, R. Freer, I.A. Kinloch, Thermoelectric power generation from lanthanum strontium titanium oxide at room temperature through the addition of graphene, ACS Appl. Mater. Interfaces 7 (29) (2015) 15898–15908.

[27] H.J. Kim, U. Kim, H.M. Kim, T.H. Kim, H.S. Mun, B.-G. Jeon, K.T. Hong, W.-J. Lee, C. Ju, K.H. Kim, High mobility in a stable transparent perovskite oxide, Appl. Phys. Express 5 (6) (2012) 061102, 061101-061103.

[28] E. Grabowska, Selected perovskite oxides: characterization, preparation and photocatalytic properties—a review, Appl. Catal. B: Environ. 186 (2016) 97–126.

[29] Y. Lin, M.T. Dylla, J.J. Kuo, J.P. Male, I.A. Kinloch, R. Freer, G.J. Snyder, Graphene/strontium titanate: approaching single crystal–like charge transport in polycrystalline oxide perovskite nanocomposites through grain boundary engineering, Adv. Funct. Mater. 30 (12) (2020) 1910071–1910077, 1910079.

[30] R.A. De Souza, The formation of equilibrium space-charge zones at grain boundaries in the perovskite oxide $SrTiO_3$, Phys. Chem. Chem. Phys. 11 (43) (2009) 9939–9969.

[31] J. Huang, P. Yan, Y. Liu, J. Xing, H. Gu, Y. Fan, W. Jiang, Simultaneously breaking the double Schottky barrier and phonon transport in $SrTiO_3$-based thermoelectric ceramics via two-step reduction, ACS Appl. Mater. Interfaces 12 (47) (2020) 52721–52730.

[32] M.T. Dylla, J.J. Kuo, I. Witting, G.J. Snyder, Grain boundary engineering nanostructured $SrTiO_3$ for thermoelectric applications, Adv. Mater. Interfaces 6 (15) (2019), 1900222-1900228.

[33] Y. Zhu, F. Azough, X. Liu, X. Zhong, M. Zhao, K. Margaronis, S. Kar-Narayan, I. Kinloch, D.J. Lewis, R. Freer, Precursor-led grain boundary engineering for superior thermoelectric performance in niobium strontium titanate, ACS Appl. Mater. Interfaces 15 (10) (2023) 13097–13107.

[34] O. Okhay, S. Zlotnik, W. Xie, K. Orlinski, M.J.H. Gallo, G. Otero-Irurueta, A. J. Fernandes, D.A. Pawlak, A. Weidenkaff, A. Tkach, Thermoelectric performance of Nb-doped $SrTiO_3$ enhanced by reduced graphene oxide and Sr deficiency cooperation, Carbon 143 (2019) 215–222.

[35] J. Cao, D. Ekren, Y. Peng, F. Azough, I.A. Kinloch, R. Freer, Modulation of charge transport at grain boundaries in $SrTiO_3$: toward a high thermoelectric power factor at room temperature, ACS Appl. Mater. Interfaces 13 (10) (2021) 11879–11890.

[36] D. Ekren, J. Cao, F. Azough, D. Kepaptsoglou, Q. Ramasse, I.A. Kinloch, R. Freer, Controlling the thermoelectric behavior of La-doped $SrTiO_3$ through processing and addition of graphene oxide, ACS Appl. Mater. Interfaces 14 (48) (2022) 53711–53723.

[37] X. Feng, Y. Fan, N. Nomura, K. Kikuchi, L. Wang, W. Jiang, A. Kawasaki, Graphene promoted oxygen vacancies in perovskite for enhanced thermoelectric properties, Carbon 112 (2017) 169–176.

[38] C. Wu, J. Li, Y. Fan, J. Xing, H. Gu, Z. Zhou, X. Lu, Q. Zhang, L. Wang, W. Jiang, The effect of reduced graphene oxide on microstructure and thermoelectric properties of Nb-doped A-site-deficient $SrTiO_3$ ceramics, J. Alloy. Compd. 786 (2019) 884–893.

[39] D. Srivastava, C. Norman, F. Azough, D. Ekren, K. Chen, M. Reece, I. Kinloch, R. Freer, Anisotropy and enhancement of thermoelectric performance of $Sr_{0.8}La_{0.067}Ti_{0.8}Nb_{0.2}O_{3-\delta}$ ceramics by graphene additions, J. Mater. Chem. A 7 (42) (2019) 24602–24613.

[40] J.U. Rahman, N. Van Du, W.H. Nam, W.H. Shin, K.H. Lee, W.S. Seo, M.H. Kim, S. Lee, Grain boundary interfaces controlled by reduced graphene oxide in nonstoichiometric $SrTiO_{3-\delta}$ thermoelectrics, Sci. Rep. 9 (1) (2019) 8624–8635.

[41] M. Wolf, K. Menekse, A. Mundstock, R. Hinterding, F. Nietschke, O. Oeckler, A. Feldhoff, Low thermal conductivity in thermoelectric oxide-based multiphase composites, J. Electron Mater. 48 (2019) 7551–7561.

[42] J. Cao, P. He, M.A. Mohammed, X. Zhao, R.J. Young, B. Derby, I.A. Kinloch, R. A. Dryfe, Two-step electrochemical intercalation and oxidation of graphite for the mass production of graphene oxide, J. Am. Chem. Soc. 139 (48) (2017) 17446–17456.

[43] A. Coelho, Whole-profile structure solution from powder diffraction data using simulated annealing, J. Appl. Crystallogr 33 (3) (2000) 899–908.

[44] L. Bokobza, J.-L. Bruneel, M. Couzi, Raman spectra of carbon-based materials (from graphite to carbon black) and of some silicone composites, C 1 (1) (2015) 77–94.

[45] C.M. Culbertson, A.T. Flak, M. Yatskin, P.H.-Y. Cheong, D.P. Cann, M.R. Dolgos, Neutron total scattering studies of group ii titanates ($ATiO_3$, A^{2+}= Mg, Ca, Sr, Ba), Sci. Rep. 10 (1) (2020) 3729, 3721-3710.

[46] R. Moos, K.H. Hardtl, Defect chemistry of donor-doped and undoped strontium titanate ceramics between 1000° and 1400 °C, J. Am. Ceram. Soc. 80 (10) (1997) 2549–2562.

[47] Wang Y., Fujinami K., Zhang R., Wan C., Wang N., Ba Y., Koumoto K. Interfacial thermal resistance and thermal conductivity in nanograined $SrTiO_3$. *Appl Phys Express.* 2010;3(3):031101: 031101-031103.

[48] S. Witek, D.M. Smyth, H. Piclup, Variability of the Sr/Ti ratio in $SrTiO_3$, J. Am. Ceram. Soc. 67 (5) (1984) 372–375.

[49] M. Aufray, S. Menuel, Y. Fort, J. Eschbach, D. Rouxel, B. Vincent, New synthesis of nanosized niobium oxides and lithium niobate particles and their characterization by XPS analysis, J. Nanosci. Nanotechnol. 9 (8) (2009) 4780–4785.

[50] D. Gonbeau, C. Guimon, G. Pfister-Guillouzo, A. Levasseur, G. Meunier, R. Dormoy, XPS study of thin films of titanium oxysulfides, Surf. Sci. 254 (1-3) (1991) 81–89.

[51] X. Liu, D. Kepaptsoglou, Z. Gao, A. Thomas, K. Maji, E. Guilmeau, F. Azough, Q. M. Ramasse, R. Freer, Controlling the thermoelectric properties of Nb-doped TiO_2 ceramics through engineering defect structures, ACS Appl. Mater. Interfaces 13 (48) (2021) 57326–57340.

[52] T. Hryniewicz, K. Rokosz, H.Z. Sandim, SEM/EDX and XPS studies of niobium after electropolishing, Appl. Surf. Sci. 263 (2012) 357–361.

[53] J. Shuai, J. Mao, S. Song, Q. Zhu, J. Sun, Y. Wang, R. He, J. Zhou, G. Chen, D. J. Singh, Tuning the carrier scattering mechanism to effectively improve the thermoelectric properties, Energy Environ. Sci. 10 (3) (2017) 799–807.

[54] Y. Wang, Y. Sui, X. Wang, W. Su, X. Liu, Enhanced high temperature thermoelectric characteristics of transition metals doped $Ca_3Co_4O_{9+\delta}$ by cold high-pressure fabrication, J. Appl. Phys. 107 (3) (2010) 033701–033709, 033708.

[55] W. Liu, H.S. Kim, S. Chen, Q. Jie, B. Lv, M. Yao, Z. Ren, C.P. Opeil, S. Wilson, C.-W. Chu, n-type thermoelectric material $Mg_2Sn_{0.75}Ge_{0.25}$ for high power generation, Proc. Natl. Acad. Sci. USA 112 (11) (2015) 3269–3274.

[56] R. Dominko, M. Gaberšček, J. Drofenik, M. Bele, J. Jamnik, Influence of carbon black distribution on performance of oxide cathodes for Li ion batteries, Electro Acta 48 (24) (2003) 3709–3716.

[57] P.C. Li, C.C. Hu, H. Noda, H. Habazaki, Synthesis and characterization of carbon black/manganese oxide air cathodes for zinc–air batteries: effects of the crystalline structure of manganese oxides, J. Power Sources 298 (2015) 102–113.

[58] J. Li, D. Li, W. Xu, X. Qin, Y. Li, J. Zhang, Enhanced thermoelectric performance of SnSe based composites with carbon black nanoinclusions, Appl. Phys. Lett. 109 (17) (2016) 173901–173904, 173902.

[59] G.J. Snyder, A.H. Snyder, M. Wood, R. Gurunathan, B.H. Snyder, C. Niu, Weighted mobility, Adv. Mater. 32 (25) (2020), 2001537-2001542.

[60] W. Wunderlich, H. Ohta, K. Koumoto, Enhanced effective mass in doped $SrTiO_3$ and related perovskites, Phys. B: Condens Matter 404 (16) (2009) 2202–2212.

[61] S. Ohta, T. Nomura, H. Ohta, K. Koumoto, High-temperature carrier transport and thermoelectric properties of heavily La-or Nb-doped $SrTiO_3$ single crystals, J. Appl. Phys. 97 (3) (2005) 034101–034104, 034106.

[62] J.J. Kuo, S.D. Kang, K. Imasato, H. Tamaki, S. Ohno, T. Kanno, G.J. Snyder, Grain boundary dominated charge transport in Mg_3Sb_2-based compounds, Energy Environ. Sci. 11 (2) (2018) 429–434.

[63] A. Markov, B. Fiedler, K. Schulte, Electrical conductivity of carbon black/fibres filled glass-fibre-reinforced thermoplastic composites, Compos - A: Appl. Sci. Manuf. 37 (9) (2006) 1390–1395.

[64] X. Liu, S. Li, J. Yu, Y. Zhu, K. Lin, B. Wang, R. Cai, D. Ekren, D. Lewis, I.A. Kinloch, M.J. Reece, R. Freer, Enhancing the thermoelectric properties of TiO_2-based ceramics through addition of carbon black and graphene oxide, Carbon (2023) 118501–118511, 118509.

[65] Z. Chen, X. Zhang, Y. Pei, Manipulation of phonon transport in thermoelectrics, Adv. Mater. 30 (17) (2018) 1705611–1705612, 1705617.

[66] R. Viennois, P. Hermet, D. Machon, M. Koza, D. Bourgogne, B. Fraisse, A. Petrovic, D. Maurin, Stability and lattice dynamics of Ruddlesden–Popper tetragonal Sr_2TiO_4, J. Phys. Chem. C. 124 (51) (2020) 27882–27893.

[67] D. Risold, B. Hallstedt, L.J. Gauckler, The strontium-oxygen system, Calphad 20 (3) (1996) 353–361.

[68] F. Azough, S.S. Jackson, D. Ekren, R. Freer, M. Molinari, S.R. Yeandel, P. M. Panchmatia, S.C. Parker, D.H. Maldonado, D.M. Kepaptsoglou, Concurrent La and A-site vacancy doping modulates the thermoelectric response of $SrTiO_3$: experimental and computational evidence, ACS Appl. Mater. Interfaces 9 (48) (2017) 41988–42000.

[69] H.S. Kim, Z.M. Gibbs, Y. Tang, H. Wang, G.J. Snyder, Characterization of Lorenz number with Seebeck coefficient measurement, APL Mater. 3 (4) (2015) 041506–041510.

[70] E.S. Toberer, A. Zevalkink, G.J. Snyder, Phonon engineering through crystal chemistry, J. Mater. Chem. 21 (40) (2011) 15843–15852.

[71] C. Wan, Y. Wang, N. Wang, W. Norimatsu, M. Kusunoki, K. Koumoto, Development of novel thermoelectric materials by reduction of lattice thermal conductivity, Sci. Technol. Adv. Mater. 11 (4) (2010) 044301–044307, 044306.

[72] T.M. Tritt, M. Subramanian, Thermoelectric materials, phenomena, and applications: a bird's eye view, MRS Bull. 31 (3) (2006) 188–198.

[73] P. Dey, S.S. Jana, F. Anjum, T. Bhattacharya, T. Maiti, Effect of semiconductor to metal transition on thermoelectric performance in oxide nanocomposites of $SrTi_{0.85}Nb_{0.15}O_3$ with graphene oxide, Appl. Mater. Today 21 (2020) 100869–100877.